



High-efficiency pollutant degradation, disinfection and H₂O₂ production activities of magnetically separable Co-imbedded N-doped carbonaceous framework/supramolecular perylene diimide photocatalyst

Lufang Ning^{a,b,c,d}, Xue Chen^{a,b,c,d}, Zhouping Wang^{a,b,c,d,e,f}, Jing Xu^{a,b,c,d,*}

^a State Key Laboratory of Food Science and Technology, Jiangnan University, Wuxi 214122, PR China

^b School of Food Science and Technology, Jiangnan University, Wuxi 214122, PR China

^c International Joint Laboratory on Food Safety, Jiangnan University, Wuxi 214122, PR China

^d Collaborative Innovation Center of Food Safety and Quality Control in Jiangsu Province, Jiangnan University, Wuxi 214122, PR China

^e National Engineering Research Center for Functional Food, Jiangnan University, Wuxi 214122, PR China

^f Key Laboratory of Meat Processing of Sichuan, Chengdu University, Chengdu 610106, PR China

ARTICLE INFO

Keywords:

Supramolecular perylene diimide photocatalyst
ZIF-67 derived co-catalyst
Pollutant degradation
Disinfection
H₂O₂ production

ABSTRACT

Herein, a magnetically separable Co-imbedded N-doped carbonaceous framework (Co-N-C)/supramolecular perylene diimide (SA-PDI) photocatalyst was prepared via an in-situ self-assembly approach. The one-dimensional (1D) SA-PDI nanofibers could sufficiently contact with the three-dimensional (3D) ZIF-67 derived porous carbon framework of Co-N-C, forming a 3D/1D heterostructure via π - π interaction and hydrogen bonding. Stable 3D porous structure, high surface area, superior conductivity and strong magnetism of Co-N-C could work as a multifunctional co-catalyst to extend the spectral-response range, increase the adsorption capacity, accelerate the charge separation efficiency and improve the recycling ability of SA-PDI. Compared to SA-PDI, Co-N-C/SA-PDI photocatalyst displayed significantly improved pollutant degradation, H₂O₂ production and disinfection activities under visible light on account of the satisfactory synergetic action between Co-N-C and SA-PDI. The degradation rates of Co-N-C/SA-PDI-70% for phenol, norfloxacin and ethylene were about 4.7, 5.2 and 3.1 times as fast as those of SA-PDI, respectively. The H₂O₂ generation of Co-N-C/SA-PDI-70% (894 $\mu\text{mol L}^{-1} \text{g}^{-1}$) was nearly 3.5 times as that of SA-PDI. Additionally, Co-N-C/SA-PDI-70% could kill 88.0% of *Staphylococcus aureus* cells within 2 h, whereas SA-PDI only inactivated 53.1%. The study provides a novel strategy to design high-efficiency SA-PDI-based photocatalysts for energy conversion and environmental remediation.

1. Introduction

The global discharge of industrial and agricultural wastewater containing phenolic pollutants (phenol and bisphenol A (BPA)), antibiotic pollutants (norfloxacin (NFX) and tetracycline (TC)), and pathogenic bacteria (*Staphylococcus aureus* (*S. aureus*)), could cause accumulative toxicity through food chain enrichment and pose a serious threat to human health, which has become a major and persistent challenge worldwide [1–5]. Additionally, as an endogenous ripening-promoted hormone, excessive ethylene in the storage atmosphere of agricultural products could result in quality deterioration of softening, browning and chlorophyll loss [6]. Therefore, the high-efficiency removal of organic hazardous compounds and pathogenic bacteria has profound practical significance in water resources protection and agricultural products

preservation. Nevertheless, traditional treatment technologies suffer from the problems of complex reaction conditions, poor persistence and harmful by-products. On the other hand, hydrogen peroxide (H₂O₂) is regarded as a promising energy source in the fields of sterilization, organic synthesis, fuel cells and wastewater treatment [7]. However, commercial anthraquinone oxidation method for industrial H₂O₂ production exists some drawbacks of complicated processes, high costs and toxic emissions [8]. In recent years, organic semiconductors based photocatalysis, as an advanced oxidation process, has attracted increasing attention in pollutant degradation, disinfection, and H₂O₂ production owing to its mild reaction condition, visible-light response, strong oxidation capacity, environmentally friendly, and diverse structural flexibility [9,10].

Perylene diimide (PDI) and its derivatives have shown considerably

* Corresponding author at: State Key Laboratory of Food Science and Technology, Jiangnan University, Wuxi 214122, PR China.

E-mail addresses: xujing823@jiangnan.edu.cn, xujing823@126.com (J. Xu).

<https://doi.org/10.1016/j.apcatb.2022.122282>

Received 28 October 2022; Received in revised form 27 November 2022; Accepted 8 December 2022

Available online 10 December 2022

0926-3373/© 2022 Elsevier B.V. All rights reserved.

photoluminescence properties, which were mainly introduced in host photocatalyst to act as the dye-sensitizers to enhance the light absorption in the early studies [11]. Nowadays, PDI has been reported as a novel organic supramolecular photocatalyst through structural adjustment to effectively overlap molecular orbitals of perylene nuclei by π - π stacking and side chain interactions, resulting in the orderly assembly of single PDI molecules into stable aggregates with appropriate energy band structures [12]. Recently, the 1D self-assembled PDI (SA-PDI) supramolecular nanofibers have been extensively investigated in the fields of light-driven degradation, disinfection and H_2O_2 production due to their unique photoelectric property, superior photo-thermal stability and suitable valence band edge potential [13–15]. However, they are still confronted with poor charge transfer efficiency, low specific surface area and difficult recovery from the reaction system. Co-catalysts decoration is a feasible modification strategy to overcome the above deficiencies of SA-PDI. On one hand, co-catalysts could combine with semiconductor to construct heterogeneous interface, thus inhibiting the recombination of photoinduced electron-hole (e^- - h^+) pairs [16]. On the other hand, they could act as surface reactive centers for the consumption of the separated photogenerated carriers so as to promote the photocatalytic reaction [17]. Furthermore, co-catalysts including noble metals, metal oxides and metal-containing complexes have been introduced into PDI system to boost photocatalytic oxidation activity, such as Pt nanoparticles [18], Pd quantum dots [19] and CoO_x [20]. Currently, Li et al. developed a novel Ti_3C_2 /PDI composite photocatalyst in which Ti_3C_2 could act as co-catalyst to enhance the electron mobility and broaden the light absorption, resulting in higher degradation rate towards tetracycline hydrochloride compared with SA-PDI [21]. Nevertheless, they still have disadvantages of recycling difficulty from the reaction system and low adsorption capacity. Therefore, how to select an ideal co-catalyst with multiple function is an important breakthrough for the development of supramolecular PDI system with rapid charge transfer, broad spectral response, high adsorption capacity and outstanding separation recyclability simultaneously.

Originated from 3D zeolite imidazole framework, ZIF-67 derivatives synthesized via pyrolysis process could realize multifunctional contents due to its multiple selectivity with tunable structure and composition, which could integrate the advantages of different constituents as well as endow the composite materials with improved optical activity, physicochemical property and interfacial function, and thus act as high-efficiency co-catalysts [22]. It was reported that the metal ions/clusters of ZIF-67 could be converted into metal atoms or metal compounds, while organic linkers could be transformed into amorphous or graphitic carbon materials through high-temperature carbonization [23]. These modified composites can be applied as efficient co-catalysts in photocatalysis, such as ZIF-67 derived $CoO_x@N$, S-C/CdS photocatalyst for H_2 evolution [24], ZIF-templated carbonized cobalt composites C-BMZIF for CO_2 reduction [25], and ZIF-67 derived carbon nanocubes/porphyrin composites for 2,4-dichlorophenol photodegradation [26]. Co-embedded N-doped polyporous carbonaceous framework (Co-N-C) derived from ZIF-67, effectively retains the parent 3D porous structure with high surface area, and simultaneously attains heteroatom doping and metallic species decoration, which has shown great chemical stability, good adsorption ability, strong magnetic response and excellent electrical conductivity [27]. Based on these advantages, we hypothesize that Co-N-C could act as a desirable co-catalyst to integrate with SA-PDI for comprehensively improving its charge transfer efficiency, spectral response range, adsorption capacity towards pollutants, and recyclability from the reaction system. Their 3D interconnected network could not only facilitate multiple reflections and scattering of incident ray, but also offer multidimensional channels for mass transport and charge transfer. The high specific surface area with abundant porosity of Co-N-C could increase the adsorption capacity and the amount reactive sites of SA-PDI. The excellent conductivity of Co-N-C could enhance the separation and transfer rate of photoinduced carriers in SA-PDI. The strong magnetism of Co-N-C could endow the

composite catalyst with magnetic separation function and good recycling performance.

Herein, Co-N-C/SA-PDI was synthesized with success via a facile in-situ self-assembly method, in which Co-N-C and SA-PDI were tightly combined for the formation of 3D/1D heterostructure. The morphological, crystal, chemical, optical and electronic characters of Co-N-C/SA-PDI were carefully investigated. The visible-light-driven catalytic activities of Co-N-C/SA-PDI were studied via pollutant degradation experiments towards phenol, antibiotics as well as ethylene, inactivation experiments towards *S. aureus* and H_2O_2 production tests. Besides, the roles of interfacial interaction, 3D/1D heterostructure, broadened spectral-response range, increased adsorption activity and accumulated reactive species played in Co-N-C/SA-PDI system were unambiguously disclosed to demonstrate the enhanced mechanism of high-efficiency photocatalytic performance via co-catalyst modification.

2. Experimental section

2.1. Synthesis of Co-N-C/SA-PDI

ZIF-67 was used as the precursor through direct pyrolysis treatment to prepare Co-N-C. The carboxy-substituent PDI (bulk PDI) molecules were synthesized according to reported method [15]. The preparation details of Co-N-C and carboxy-substituent PDI were described in the [Supplementary Material](#). Co-N-C/SA-PDI was prepared through an in-situ self-assembly strategy. Firstly, 100 mg bulk PDI was added to 37 mL ultrapure water with the following addition of 151 μ L triethylamine under vigorous stirring to form dark red PDI solution (5 mM). 4.71 mL HCl solution (4 M) was added to above obtained suspension with stirring for 1 h to achieve a SA-PDI dispersion. Subsequently, a certain volume of Co-N-C dispersion (10 mg/mL) was added and stirred for 1 h at 60 °C, followed by ultrasound for 1 h. Finally, as-prepared mixture was filtered and washed with ultrapure water to neutral. The obtained powder was dried in a vacuum at 60 °C. A series of resultant composites was marked as Co-N-C/SA-PDI-X, X meant the mass ratio of SA-PDI in the composite system, X = 50%, 60%, 70%, 80%, 90%.

2.2. Photocatalytic degradation experiments

Phenol, BPA, NFX, TC and ethylene were used as the targets to evaluate the pollutant degradation activity of as-synthesized materials. More details were described in the [Supplementary Material](#).

2.3. Photocatalytic antibacterial experiments

Gram-positive *Staphylococcus aureus* (*S. aureus*) cells were used to evaluate the antibacterial activity of as-synthesized materials. More details were described in the [Supplementary Material](#).

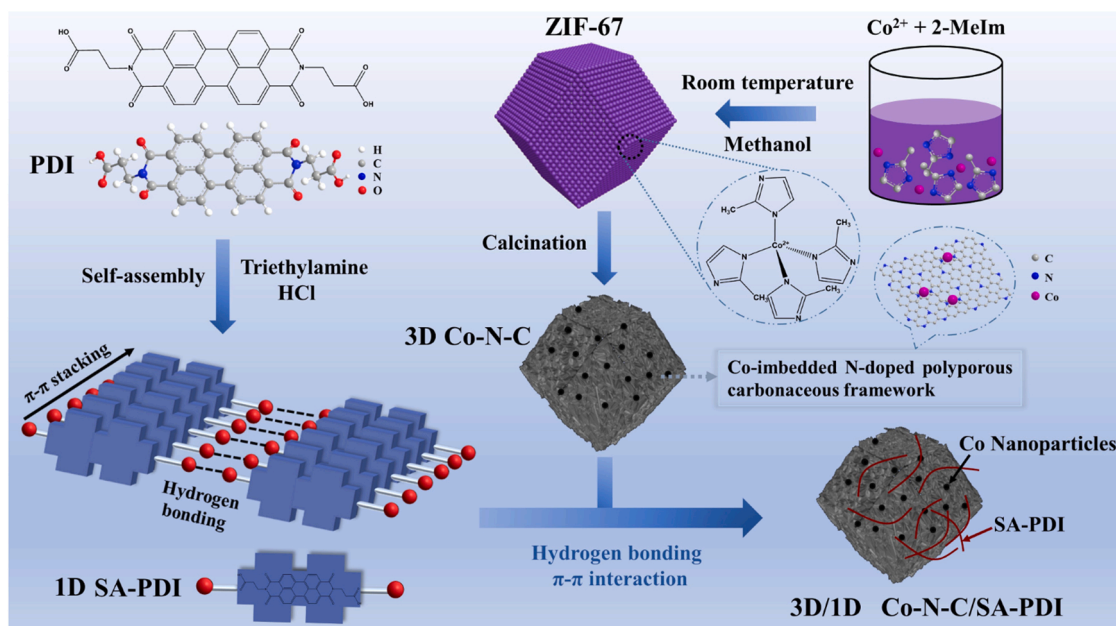
2.4. Photocatalytic H_2O_2 production experiments

The details were illustrated in the [Supplementary Material](#).

3. Results and discussion

3.1. The heterostructure of Co-N-C/SA-PDI photocatalyst

The preparation route of Co-N-C/SA-PDI heterostructure was shown in [Scheme 1](#). Bulk PDI was initially dissolved in an alkaline solution of triethylamine and followed self-assembled into SA-PDI supramolecular nanofibers after the addition of hydrochloric acid. Co-N-C co-catalyst was originated from high-temperature pyrolysis of ZIF-67, generating N-doping Co nanoparticles-embedded polyporous carbonaceous skeleton. Subsequently, SA-PDI and Co-N-C were combined to Co-N-C/SA-PDI by an in-situ self-assembly strategy. 3D matrix of Co-N-C was intimately contacted with 1D SA-PDI nanofibers, constructing stable 3D/1D



Scheme 1. The preparation route of Co-N-C/SA-PDI photocatalyst.

heterostructure. What's more, the zeta potentials of SA-PDI and Co-N-C are -33.9 mV and -8.1 mV, respectively, suggesting they cannot be compounded via electrostatic attraction (Fig. S1). On account of the π -electron conjugation system and carboxyl groups of SA-PDI, we make a reasonable speculation that it can make a tight integration with N-rich porous carbonaceous skeleton of Co-N-C via hydrogen bonding and π - π interaction. As a result, the combination of SA-PDI and Co-N-C makes the zeta potential of Co-N-C/SA-PDI-70% change into -27.1 mV (Fig. S1).

Transmission electron microscopy (TEM), scanning electron microscopy (SEM) and high-resolution TEM (HRTEM) were carried out to observe the morphologies of SA-PDI, Co-N-C and Co-N-C/SA-PDI. SA-PDI exhibits a 1D irregular nanofiber-like structure with a length of ~ 200 – 500 nm and a diameter of ~ 30 nm (Figs. 1a and 2a). After undergoing the carbonization of ZIF-67 in inert atmosphere, Co-N-C frameworks display rhombic dodecahedral structures with sizes on the scale of 400 – 500 nm, which possess imbedded Co nanoparticles with the lattice fringe of 0.21 nm, rough surfaces and wrinkled concave shapes (Figs. 1b, 2b and S2). The homogeneous dispersion of Co nanoparticles in the carbon matrix enables the adequate interfacial connection between two constituents, resulting in the strong conductivity [28]. Co-N-C/SA-PDI-70% maintains the original 3D framework during the compounding process, and it can be observed that SA-PDI nanofibers are

loaded at the edge of Co-N-C framework, suggesting the close combination of these two components and the successful formation of 3D/1D heterostructure (Figs. 1c and 2c).

Thermal gravimetric analysis (TGA) presents that Co-N-C/SA-PDI-70% shows a gradual weight loss in the range of 350 °C– 650 °C due to the cleavage of amide-site side chains in PDI skeleton as well as the decomposition of partial ligands in Co-N-C framework, indicating the composite still performs good thermal stability (Fig. S3). As Co-N-C/SA-PDI-70% displays the middle thermal decomposition temperature and weight loss rate between the two, verifying that Co-N-C successfully combined with SA-PDI. What's more, compared to SA-PDI, Co-N-C/SA-PDI-70% exhibits higher pore volume (0.27 cm³ g⁻¹) and larger surface area (120.45 m² g⁻¹) due to the modification of 3D polyporous structure of Co-N-C co-catalyst. Co-N-C/SA-PDI-70% also shows type-IV isotherms with a type H3 hysteresis loop and a pore-size distribution in 2 – 20 nm, manifesting its mesoporous characteristics (Fig. S4 and Table S2). Combining the above analysis, it can be found that 3D/1D Co-N-C/SA-PDI heterostructure was successfully constructed with excellent thermal stability, enhanced specific surface area and superior nanoporous property, which can provide more reaction active sites and facilitate fast electron migration and mass transfer, thus promoting the overall photocatalytic process [29].

The crystalline phase, chemical bond and light absorption property

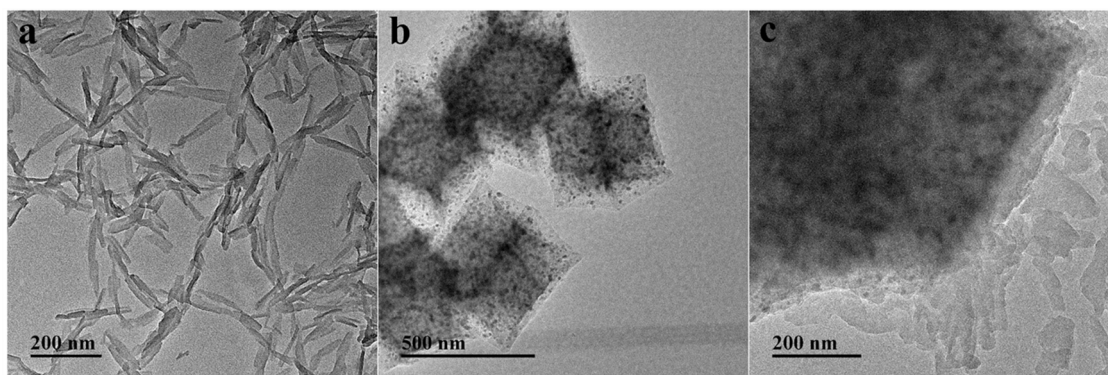


Fig. 1. TEM images of (a) SA-PDI, (b) Co-N-C, and (c) Co-N-C/SA-PDI-70%.

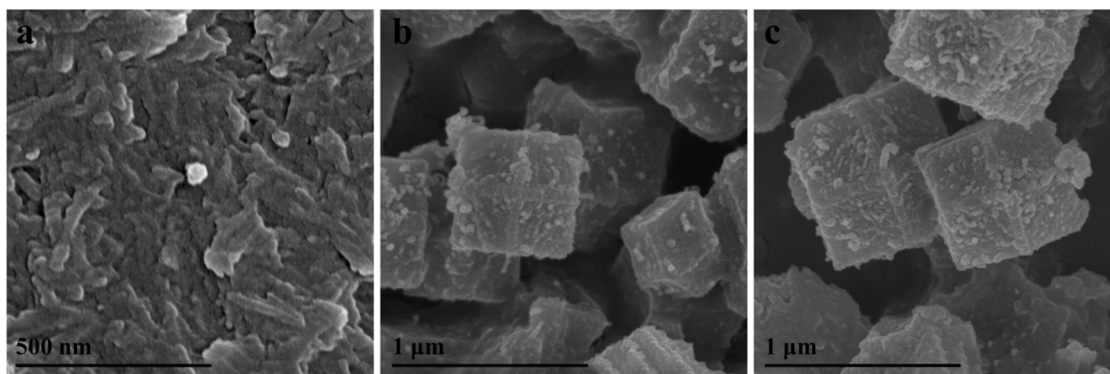


Fig. 2. SEM images of (a) SA-PDI, (b) Co-N-C, and (c) Co-N-C/SA-PDI-70%.

of Co-N-C/SA-PDI were measured by X-ray diffractometer (XRD), Raman spectroscopy, Fourier transform infrared (FTIR) spectroscopy and diffuse reflection spectra (DRS) analysis. As shown in the XRD pattern (Fig. 3a), the two characteristic peaks at 44.4° and 51.6° of Co-N-C are corresponding to the (111) and (200) facet of metallic cobalt nanoparticles, respectively [26]. SA-PDI shows several sharp diffraction peaks in the range of 10° – 27° , indicating its high crystallinity. The peak of SA-PDI at 26.1° is assigned to π - π stacking, and its intensity ratio to the peak at 14.2° ($I_{26.1}/I_{14.2}$) is greater than 1, suggesting that the highly ordered π - π stacking structure of SA-PDI [15]. As mass fraction of Co-N-C increases, the intensities of diffraction peaks indexed to SA-PDI in Co-N-C/SA-PDI composites become less evident, while the characteristic

peaks of Co-N-C are gradually strengthened. What's more, the $I_{26.1}/I_{14.2}$ value of Co-N-C/SA-PDI has a positive correlation with the rising amount of SA-PDI, indicating the heterostructure is beneficial to the π - π stacking in between and thus promoting the interlayer transfer of photogenerated electrons.

As observed in the Raman spectra (Fig. 3b), two obvious peaks at 1341 cm^{-1} and 1588 cm^{-1} of Co-N-C are in line with disordered sp^2 -bonded carbon and ordered pyrolytic graphite, respectively [26]. The peak at 1587 cm^{-1} of SA-PDI attributed to the stretching vibration of in-plane C=C/C-C is sensitive to the π - π stacking, while the peak at 1297 cm^{-1} corresponding to the bending vibration of in plane C-H is insensitive to the π - π stacking. Hence, the degree of ordered π - π stacking

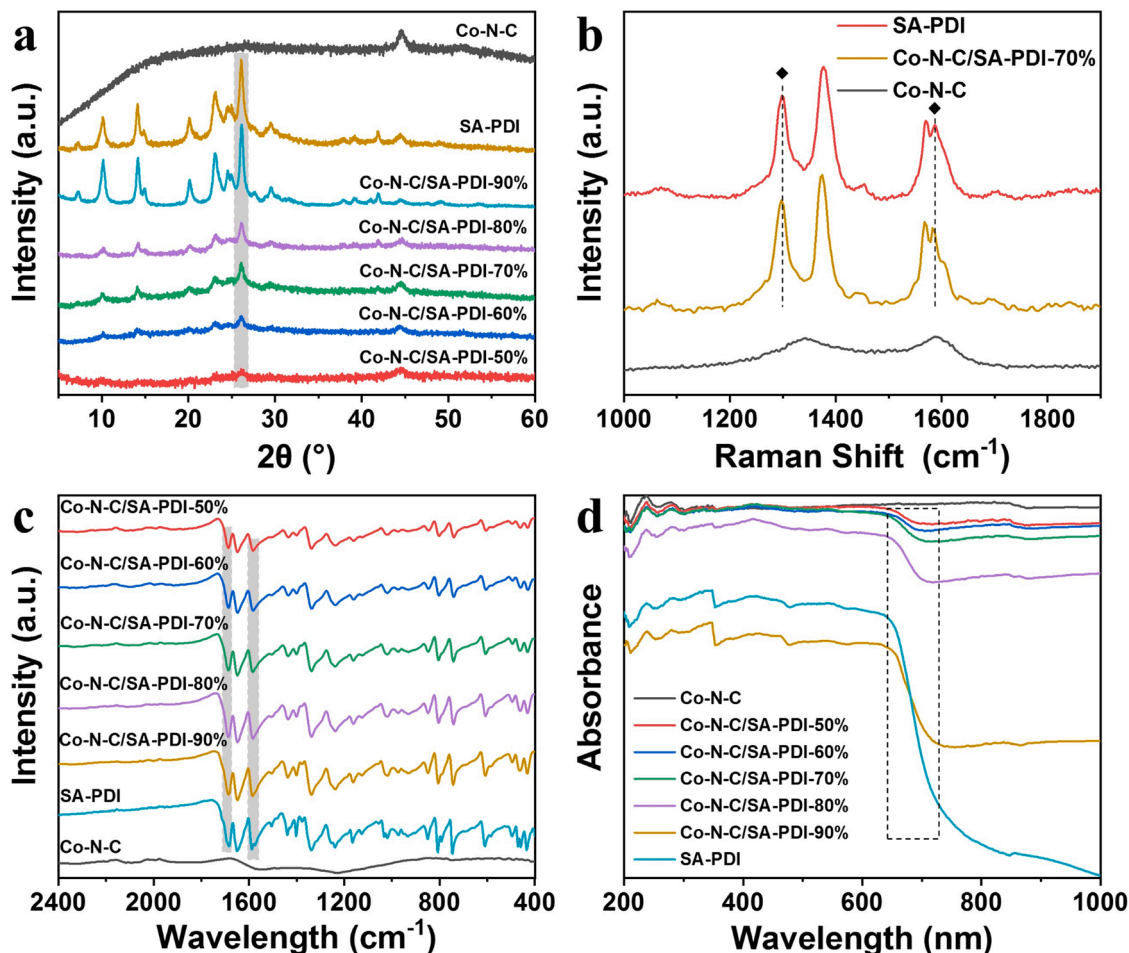


Fig. 3. (a) XRD, (b) Raman, (c) FTIR and (d) DRS analysis of SA-PDI, Co-N-C and Co-N-C/SA-PDI.

can be evaluated by the intensity ratio of 1587 cm^{-1} and 1297 cm^{-1} (I_{1587}/I_{1297}) [30]. It turns out that the I_{1587}/I_{1297} value of Co-N-C/SA-PDI-70% (0.746) is observed to be slightly higher than that of SA-PDI (0.710), suggesting enhanced degree of π - π stacking in the heterostructure as a result of the similar π -conjugated structure in two components. Moreover, Raman peaks of Co-N-C/SA-PDI-70% slightly shift towards lower wavenumbers compared to that of SA-PDI, which could also be an evidence of π - π interaction existed in between.

Fig. 3c shows that FTIR peaks at 1253 cm^{-1} and 1591 cm^{-1} of Co-N-C are related to stretching vibrations of C-N and C=C, respectively, suggesting basically sustaining 3D carbon frameworks. The peaks of SA-PDI at 1685 cm^{-1} , 1648 cm^{-1} , 1585 cm^{-1} , and 744 cm^{-1} belong to the stretching vibration of C=O, C=C, O-H and the bending vibration of O=CN-, respectively, suggesting the presence of benzene ring and carboxyl-substituent group [31]. In the composite, the C=O and O-H stretching peaks of composites make a slight shift compared with SA-PDI, indicating the existence of hydrogen bonding between SA-PDI and Co-N-C.

UV-Vis DRS of the as-prepared samples are displayed in Fig. 3d. SA-PDI shows light absorbance covering the whole visible region, and Co-N-C exhibits stronger and wider light absorption on account of the multiple reflections and scattering of incident ray in its 3D nanoporous carbonaceous framework [26]. Moreover, the rising addition of Co-N-C in the composite could gradually broaden the spectral response region and boost the light absorption ability of the composite. Based on the Tauc-Plot method, the band gap energy (E_g) of SA-PDI and Co-N-C/SA-PDI-70% are ca. 1.77 eV and 1.43 eV, respectively (Fig. S5). The raised light-harvesting ability as well as narrower E_g of Co-N-C/SA-PDI is favorable for the solar energy utilization, which can produce more photoinduced charges took part in the catalytic process.

X-ray photoelectron spectroscopy (XPS) and elemental analysis were used to study the chemical state and elemental compositions of Co-N-C/SA-PDI. In the survey spectra (Fig. S6), SA-PDI shows the presence of C, N and O elements, while Co-N-C and Co-N-C/SA-PDI-70% is comprised of C, N, O and Co elements. The elemental analysis demonstrates that Co-N-C shows the largest N content, SA-PDI has the largest C and O contents, and the individual atomic content of C, N and O in Co-N-C/SA-PDI-70% is between the two components (Table 1). The C 1s spectrum of Co-N-C/SA-PDI-70% (Fig. 4a) reveals the presence of four peaks at 284.8, 285.9, 287.9 and 289.2 eV originated from the carbonaceous motif of SA-PDI and Co-N-C, which are associated with C-C, C-N/C=N, C-O and π -excitation [13,25]. The N 1s spectrum of Co-N-C/SA-PDI-70% (Fig. 4b) shows four peaks at 398.6, 399.2, 400.2 and 401.1 eV, which are assigned to pyridinic-N, Co-N, C-N/pyrrolic-N and graphitic-N, respectively [32,33]. Compared to SA-PDI and Co-N-C, the dominant N species peaks in Co-N-C/SA-PDI-70% shift towards higher binding energy, implying the existence of π - π interaction in between. Besides, N doping in the carbonaceous matrix could affect the adjacent carbon atoms by altering electron spin density and charge distribution, producing a surface activation region and then promoting the electron transfer from SA-PDI to N-rich carbonaceous substrates of Co-N-C [34]. The O 1s spectrum of Co-N-C/SA-PDI-70% (Fig. 4c) exhibits four peaks at 530.3, 531.1, 532.0 and 533.4 eV, which are related to Co-O, C=O, C-O-C and adsorbed H_2O , respectively [35,36]. Compared with SA-PDI, the peaks of C=O, C-O-C and adsorbed H_2O in Co-N-C/SA-PDI-70% move to lower binding energy, suggesting enhance surface electron density because of the π - π interaction and carriers migration along Co-N-C and SA-PDI [31]. There are two predominant peaks in the Co 2p

spectrum of Co-N-C/SA-PDI-70%, Co $2p_{1/2}$ and Co $2p_{3/2}$ (Fig. 4d). Co $2p_{1/2}$ is resolved into three forms centered at 793.3 eV, 796.3 eV and 802.1 eV, matching with Co $2p_{1/2}\text{ Co}^0$, Co $2p_{1/2}\text{ Co}^{2+}$ and satellite peak, respectively. Co $2p_{3/2}$ is deconvoluted into three forms centered at 778.2 eV, 780.6 eV and 785.4 eV, matching with Co $2p_{3/2}\text{ Co}^0$, Co $2p_{3/2}\text{ Co}^{2+}$ and satellite peak, respectively [37]. The imbedded Co nanoparticles can offer electron traps to improve electron transport of Co-N-C/SA-PDI due to their abilities on altering Fermi energy level. Partial retained N-coordinated and surface oxidized cobalt species could result in Co^{2+} phases [26]. Additionally, the lower binding energy of above cobalt peaks of Co-N-C/SA-PDI-70% compared with Co-N-C could be an evidence of interfacial carriers migration in between.

According to the above analysis, the schematic of inner interactions between SA-PDI and Co-N-C in 3D/1D composite system is illustrated in Scheme 2. Firstly, bulk PDI is self-assembled into supramolecular nanofibers by π - π stacking and hydrogen bonds. Then SA-PDI nanofibers are closely contacted with N-rich porous carbonaceous skeleton of Co-N-C to form 3D/1D heterostructure by π - π interaction and hydrogen bonds. The existed strong interactions are benefiting the interlayer and interfacial carriers transport, and thus promoting the catalytic activity of Co-N-C/SA-PDI under visible light.

3.2. High-efficiency visible light-driven catalytic performances of Co-N-C/SA-PDI system

The photocatalytic activities of Co-N-C/SA-PDI heterostructure are tested via pollutant degradation, H_2O_2 production as well as disinfection experiments. Phenolic pollutants involving phenol and BPA, antibiotic pollutants including NFX and TC, and gaseous ethylene are chosen as the targets of photodegradation reaction. It took near 1 h to get the adsorption-desorption equilibrium, and about 6.8%, 10.5% and 14.8% of phenol were adsorbed by SA-PDI, Co-N-C/SA-PDI-70% and Co-N-C, respectively (Fig. S7a). This suggests that 3D network structure with large surface area as well as nanoporous property of Co-N-C is beneficial to enhance adsorption capability and mass diffusion of Co-N-C/SA-PDI, which is vital to subsequent catalytic oxidation reaction [30,38]. Fig. S7b shows the comparison of phenol degradation over SA-PDI, Co-N-C, Co-N-C/SA-PDI composites, the physical mixing composite, as well as the common visible-light photocatalyst, $\text{g-C}_3\text{N}_4$. Co-N-C, $\text{g-C}_3\text{N}_4$, 70%-physical mixing sample and SA-PDI exhibit poor photodegradation activities, only 6.6%, 13.9%, 19.8% and 25.6% of phenol are removed within 100 min visible light irradiation, respectively. On the contrary, the degradation rates of Co-N-C/SA-PDI with different mass ratios have been remarkably enhanced. Co-N-C/SA-PDI-70% possesses the optimum removal efficiency among all the composites, which can degrade about 73.1% of phenol within 100 min. According to the first-order kinetic fitting curves (Fig. S7c) [39,40], the apparent rate constant (k) of Co-N-C/SA-PDI-70% (0.0131 min^{-1}) is almost 20.4, 4.7 and 9.0 times higher than that of Co-N-C (0.0006 min^{-1}), SA-PDI (0.0027 min^{-1}) and $\text{g-C}_3\text{N}_4$ (0.0014 min^{-1}) (Fig. 5a). Meanwhile, the degradation efficiency has a negative correlation with the increasing content of Co-N-C in the composite as the mass ratio of SA-PDI decreases from 70% to 50%, which might be ascribed to reduced reactive sites and extended electron transport path caused by the decoration of excessive Co-N-C co-catalyst [41]. This reveals that the noticeably reinforced photocatalytic degradation activity in Co-N-C/SA-PDI can be ascribed to strong synergistic action between Co-N-C and SA-PDI. The effect of imbedded Co nanoparticles in the heterostructure on photocatalytic performance was investigated via the decoration of acid-etched Co-N-C treated by different HCl solution concentrations. The retained Co content of samples were summarized in Table S3. As shown in Figs. S7d and 5b, the as-prepared composites with decreasing amount of Co nanoparticles exhibit gradually declined k towards phenol degradation. The determined k values of Co-N-C(1 M HCl)/SA-PDI-70% and Co-N-C(10 M HCl)/SA-PDI-70% were 0.0040 min^{-1} and 0.0029 min^{-1} , which were reduced to approximately 30.5% and 22.1% of Co-N-C/SA-PDI-70%,

Table 1
The elemental analysis results of SA-PDI, Co-N-C and Co-N-C/SA-PDI-70%.

| Sample | C (wt%) | N (wt%) | H (wt%) | O (wt%) | Co (wt%) |
|-------------------|---------|---------|---------|---------|----------|
| SA-PDI | 65.58 | 5.07 | 3.21 | 26.14 | — |
| Co-N-C | 41.31 | 9.99 | 1.61 | 22.06 | 25.03 |
| Co-N-C/SA-PDI-70% | 61.39 | 6.93 | 2.89 | 24.99 | 3.80 |

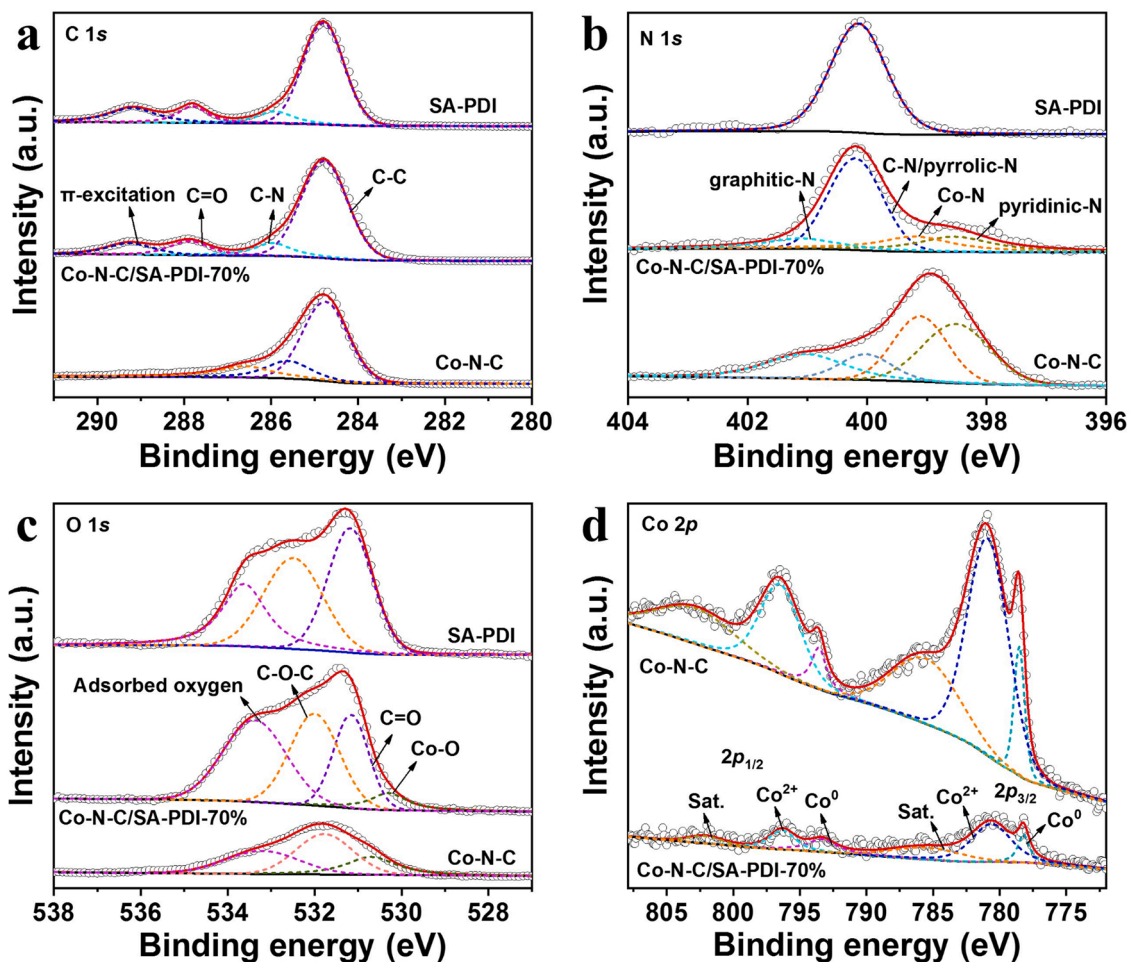
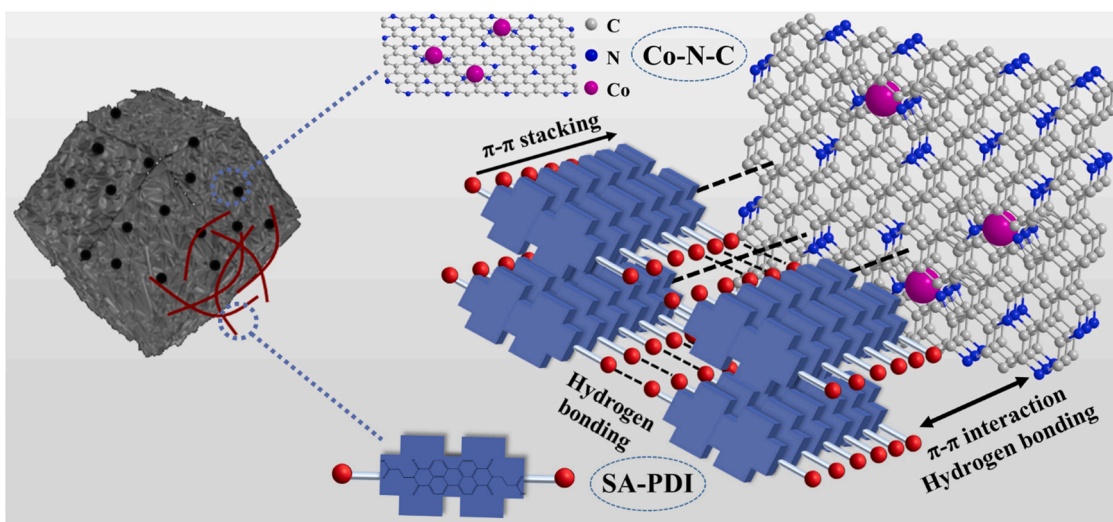


Fig. 4. (a) XPS C 1s, (b) N 1s and (c) O 1s spectra of SA-PDI, Co-N-C/SA-PDI-70% and Co-N-C. (d) XPS Co 2p spectra of Co-N-C/SA-PDI-70% and Co-N-C.



Scheme 2. The interactions between SA-PDI and Co-N-C in composite system.

respectively, suggesting that imbedded Co nanoparticles in Co-N-C/SA-PDI are conducive to suppressing the recombination of e^-h^+ pairs and improving the photocatalytic performance. Fig. S8 displayed the HPLC chromatograms towards phenol. Co-N-C/SA-PDI-70% exhibits more significantly weakened phenol peak at 4.1 min and more pronounced varied intermediate peaks during 1.0–3.5 min with time

extending than SA-PDI, demonstrating that degradation and mineralization reactions happen synchronously in the organic pollutants removal processes. Under the attack of various reactive species formed by the heterostructure, the phenol molecules could be mineralized into various aromatic intermediates (such as p-benzoquinone and hydroquinone), further oxidized into lower fatty acids, and eventually

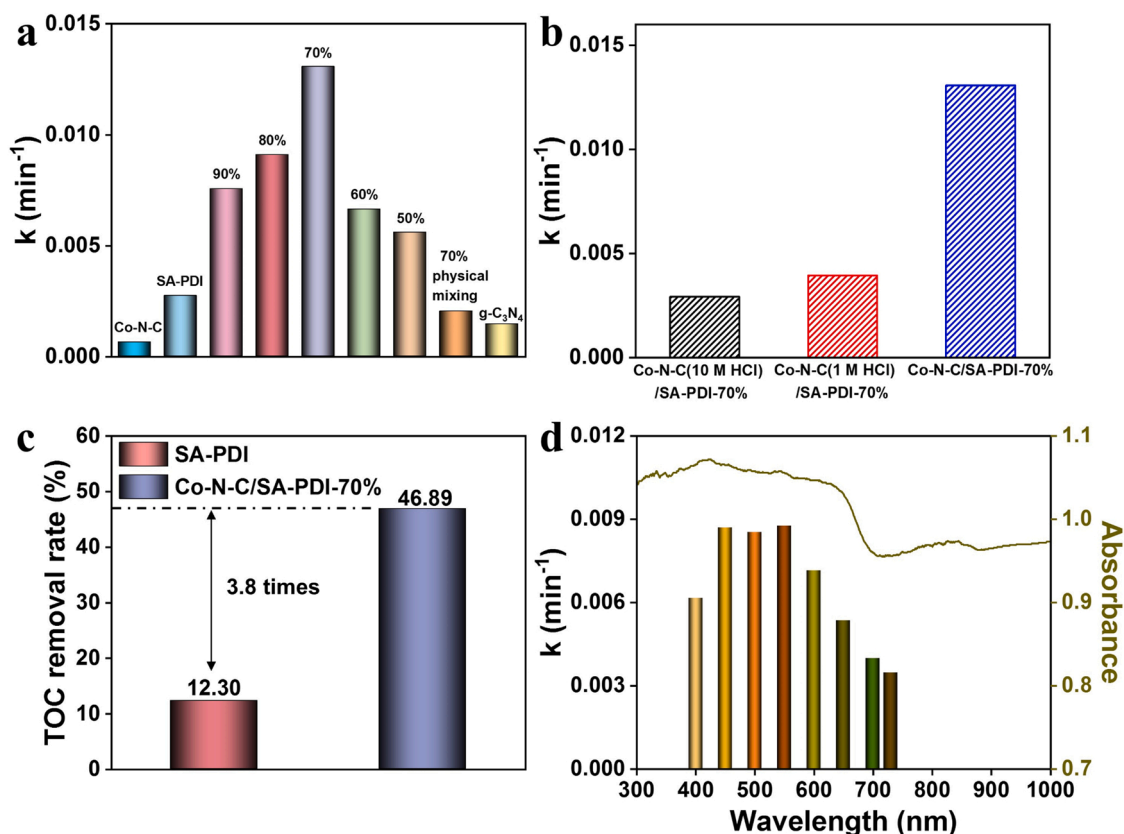


Fig. 5. (a) The apparent rate constants (k) for phenol degradation of SA-PDI, Co-N-C, Co-N-C/SA-PDI, 70%-physical mixing and g-C₃N₄ under visible-light. (b) The k values for phenol photodegradation of Co-N-C/SA-PDI-70% and acid-etched Co-N-C/SA-PDI-70%. (c) The TOC removal rate towards phenol of SA-PDI and Co-N-C/SA-PDI-70%. (d) The k values for phenol photodegradation of Co-N-C/SA-PDI-70% at different wavelengths.

decomposed into CO₂ and H₂O via ring-opening reactions [15]. Furthermore, total organic carbon (TOC) analysis was conducted to evaluate the mineralization ability of as-synthesized photocatalysts (Fig. 5c). After 3 h of phenol degradation, the TOC removal rate of Co-N-C/SA-PDI-70% is 46.89%, which is nearly 3.8 times as that of SA-PDI (12.30%), revealing that the mineralization ability of the composite has been enhanced with the increasing degradation activity. Additionally, as shown in Fig. 5d, the variation tendency of monochromatic-light wavelength-dependent k values of Co-N-C/SA-PDI-70% is in strong consistent with DRS curve, implying that the light absorption acts a pivotal part in the photocatalytic reaction. We can observe that higher degradation rates are primarily centered in the visible light region, manifesting the more effective visible light utilization of Co-N-C/SA-PDI-70%. Besides, Co-N-C/SA-PDI-70% also exhibits certain degradation efficiency in the near infrared region, suggesting that tightly integration with Co-N-C co-catalyst is able to enlarge spectral response range of the composite, effectively increase solar light utilization and thus boost full-spectrum photocatalytic activity.

The universality of visible-light degradation activity of Co-N-C/SA-PDI photocatalyst was also studied towards other organic pollutants (Fig. S9). Among as-synthesized samples, Co-N-C/SA-PDI-70% always shows the highest determined k values for BPA, NFX, TC and ethylene photodegradation, which are nearly 6.8, 5.2, 2.4 and 3.1 times as those of SA-PDI, respectively, and almost 17.0, 34.6, 6.2 and 6.3 times as those of Co-N-C, respectively (Fig. 6a). Moreover, UPLC-Q-TOF MS analysis was carried out to identify transformation intermediates (P1-P10) of NFX photodegradation using Co-N-C/SA-PDI-70% (Fig. S10). As shown in Fig. S11, three pathways of NFX degradation in the photocatalytic process were proposed as follows: decarboxylation (path I), defluorination (path II) and piperazine ring conversion (path III) [42–44]. Based on the aforementioned degradation pathway, NFX molecules can be

oxidized into small molecules through hydroxyl substitution, structural reorganization and ring-opening cleavage processes under the attack of reactive species. The opening and cleavage of piperazine ring further indicate that Co-N-C/SA-PDI exhibits strong oxidation capacity and mineralization ability. The stability of Co-N-C/SA-PDI system was evaluated through recycle tests of ethylene photodegradation. It can be found that Co-N-C/SA-PDI-70% still exhibits high catalytic efficiency with a decrease of 4.3% after five cycles, suggesting the good stability of Co-N-C/SA-PDI photocatalyst (Fig. S12). Besides, the structure of Co-N-C/SA-PDI-70% after the photocatalytic reaction is basically similar to the original one, further proving the composite is quite stable in photocatalytic reactions (Fig. S13).

Moreover, the H₂O₂ production activity using phenol as the sacrificial agent was studied to confirm the boosted photocatalytic performance of Co-N-C/SA-PDI under visible light. According to the standard curve of absorbance-H₂O₂ concentration (Fig. S14), Co-N-C shows negligible H₂O₂ production, by contrast, the accumulation H₂O₂ concentration produced within 2 h by Co-N-C/SA-PDI-70% is 894 $\mu\text{mol L}^{-1}$ g⁻¹, which is nearly 3.5 times as that of SA-PDI (257 $\mu\text{mol L}^{-1}$ g⁻¹) (Fig. 6b). Since Co-N-C/SA-PDI exhibits satisfactory H₂O₂ production ability in phenol degradation system, the Co²⁺ species existed in Co-N-C could react with in-situ generated H₂O₂ to form hydroxyl radicals ($\bullet\text{OH}$), thus giving rise to the photocatalysis-self-Fenton reaction for highly effective removal of organic pollutants [45].

Furthermore, *Staphylococcus aureus* (*S. aureus*) was selected as the target bacteria to investigate disinfection activity of Co-N-C/SA-PDI (Fig. S15). Few *S. aureus* cells can be killed in both light and dark control groups, indicating either visible light or the composite itself has no antibacterial effect on *S. aureus* cells (Fig. 6c). The bactericidal efficiency of Co-N-C/SA-PDI-70% within 2 h (88.0%) is significantly higher than that of SA-PDI (53.1%) and Co-N-C (33.9%) under visible light.

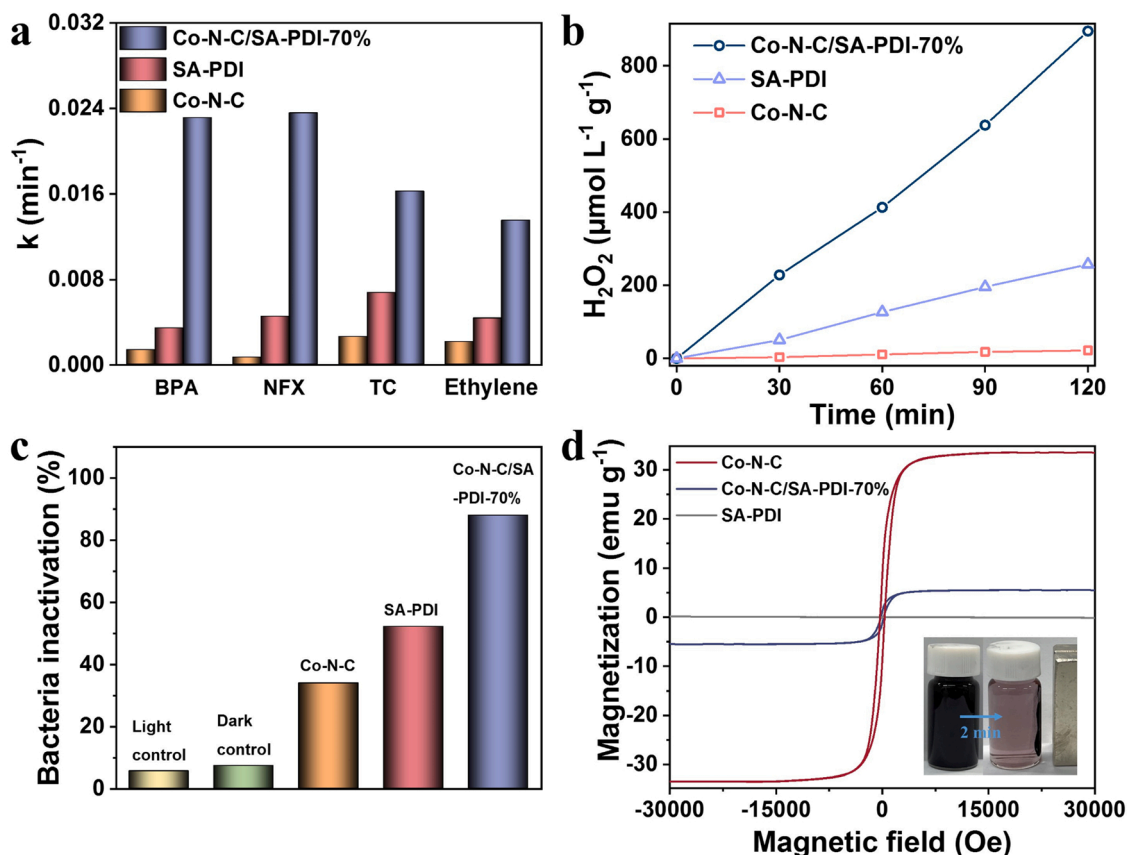


Fig. 6. (a) The k values for various pollutants degradation, (b) the photocatalytic H_2O_2 generation curves, (c) the photocatalytic inactivation rate for *S. aureus* cells, and (d) the magnetic hysteresis loops at 300 K of SA-PDI, Co-N-C and Co-N-C/SA-PDI-70% (the inset exhibits the magnetically separable function of Co-N-C/SA-PDI-70%).

Additionally, the morphological change of *S. aureus* cells after the disinfection was investigated via SEM analysis (Fig. S16). The original smooth membrane of *S. aureus* has been evidently damaged by reactive species generated in the composite system. The deformed *S. aureus* cells display a mass of folds, pits and holes on the surface, resulting in the leakage of cellular contents and inactivation of bacteria [41,46].

In short, Co-N-C/SA-PDI displays excellent pollutant degradation, H_2O_2 production and disinfection activities, indicating it possesses broad application prospects in water treatment, environmental purification and food safety. Considerably improved photocatalytic performance of Co-N-C/SA-PDI is owing to strong synergistic action between SA-PDI and Co-N-C co-catalyst. Besides, metallic Co nanoparticles imbedded in Co-N-C endow the heterostructure superparamagnetic property. Compared to SA-PDI, Co-N-C/SA-PDI-70% exhibits stronger magnetic response and achieves fast magnetic separation within 2 min (Fig. 6d), indicating the good recoverability of the composite catalyst in practice.

3.3. Enhancement mechanism of photocatalytic activity of Co-N-C/SA-PDI

The dynamic behavior of photogenerated carriers in Co-N-C/SA-PDI was studied via fluorescence spectroscopy and photoelectrochemistry analysis. The photoluminescence (PL) spectra (Fig. 7a) shows that Co-N-C has no obvious emission peak, whereas SA-PDI and Co-N-C/SA-PDI-70% both display an emission peak at 642 nm. Compared to SA-PDI, there is an evident fluorescence quenching in Co-N-C/SA-PDI-70%, indicating the effective suppressed charge recombination rate after the modification of Co-N-C co-catalyst [30]. According to the bi-exponential fitting result of transient fluorescence spectra (Fig. 7b and Table 2), the

fluorescence lifetimes of charge carriers (τ_{ave}) for SA-PDI and Co-N-C/SA-PDI-70% are ca. 8.72 ns and 6.50 ns, respectively. The shorter lifetime of the composite might be related to the existence of a non-radiative pathway on account of the electronic interaction between SA-PDI and Co-N-C [47]. As shown in Table 2, non-radiative transfer rate constant (k_{ent}) is calculated based on the equation $k_{\text{ent}} = \langle \tau_1 \rangle^{-1} - \langle \tau_2 \rangle^{-1}$. The $\langle k_{\text{ent}} \rangle$ of Co-N-C/SA-PDI-70% (0.16 ns^{-1}) is 1.45 times as that of SA-PDI (0.11 ns^{-1}). And the electron transfer rate constant (k_{et}) of Co-N-C/SA-PDI-70% is calculated to be 0.04 ns^{-1} by the equation $k_{\text{et}} = \langle \tau(\text{Co-N-C/SA-PDI-70\%}) \rangle^{-1} - \langle \tau(\text{SA-PDI}) \rangle^{-1}$, indicating the heterostructure can promote the interfacial energy transfer and electron transfer rates [48,49]. Due to the outstanding electrical conductivity of N-doped carbonaceous matrix and imbedded Co nanoparticles, Co-N-C co-catalyst is conducive to boosting the photoelectric conversion property of composite photocatalyst [50]. The photocurrent response of Co-N-C/SA-PDI-70% under visible light is almost 3.3 and 1.6 times as high as that of SA-PDI and Co-N-C, respectively (Fig. 7c). After turning on the light, the instantaneous photocurrent signal of Co-N-C/SA-PDI-70% increases quickly at first and then decreases, which might on account of the charge and discharge of electric double layer in the electrode polarization process [26]. As shown in Fig. 7d, among three samples, Co-N-C/SA-PDI-70% shows the smallest arc radius of electrochemical impedance spectroscopy (EIS) Nyquist plots, which is in line with its lowest charge transfer resistance (R_{ct}) on the basis of the fitting results of equivalent circuit (Table S4) under visible light [10]. As a result, higher photocurrent and lower resistance of Co-N-C/SA-PDI-70% suggest faster photogenerated charge transfer as well as lower recombination of e^-h^+ pairs, thus promoting the photocatalytic reaction efficiency [41,51].

To investigate the contributions of various reactive species towards

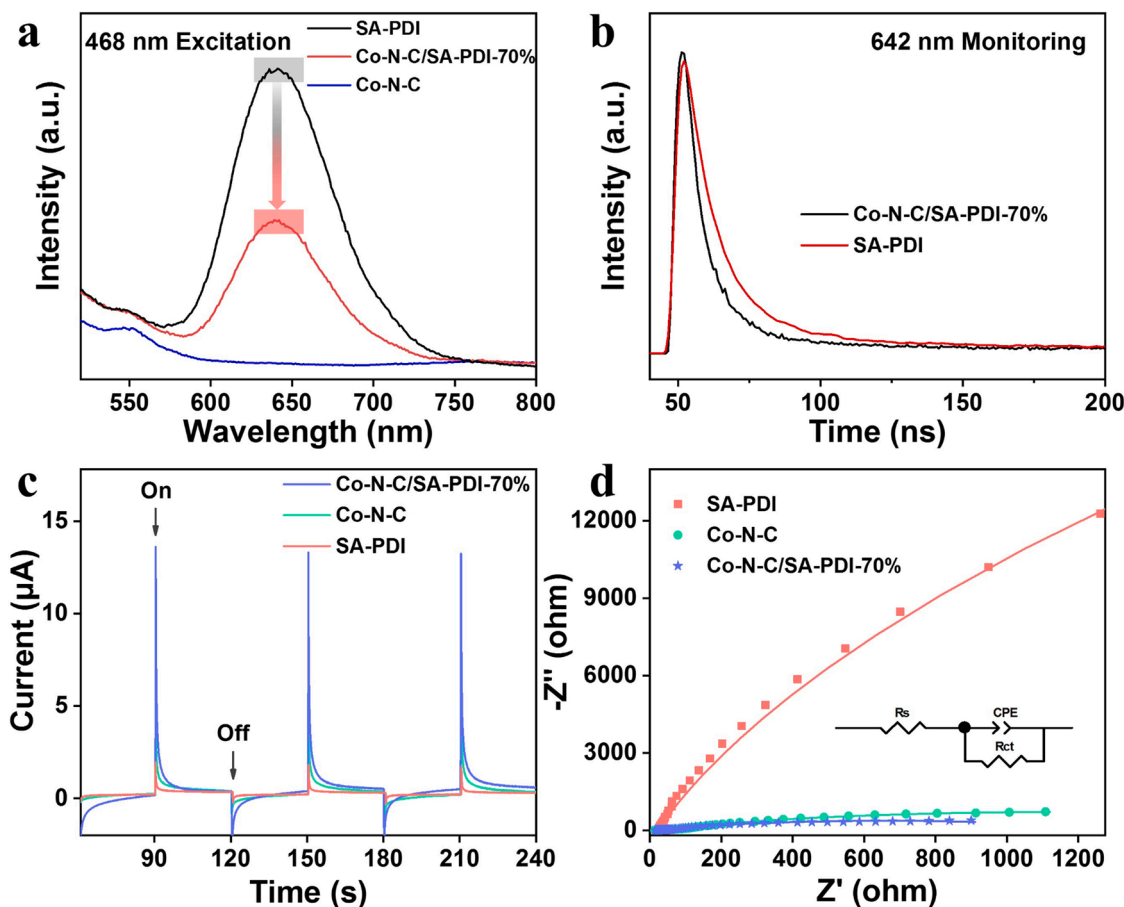


Fig. 7. (a) PL emission spectra of SA-PDI, Co-N-C and Co-N-C/SA-PDI-70%, (b) transient fluorescence spectra under 468 nm excitation of SA-PDI and Co-N-C/SA-PDI-70%, (c) photocurrent response curves and (d) EIS Nyquist plots under visible light (the inset shows the fitted equivalent circuit) of SA-PDI, Co-N-C and Co-N-C/SA-PDI-70%.

Table 2

The fluorescence lifetimes of SA-PDI and Co-N-C/SA-PDI-70%.

| Sample | τ_1 (ns) | A_1 | τ_2 (ns) | A_2 | τ_{ave} (ns) | k_{ent} (ns ⁻¹) | k_{et} (ns ⁻¹) |
|-------------------|---------------|---------|---------------|-------|-------------------|-------------------------------|------------------------------|
| SA-PDI | 8.30 | 3045.46 | 100.92 | 1.14 | 8.72 | 0.11 | – |
| Co-N-C/SA-PDI-70% | 5.74 | 2803.21 | 92.54 | 1.52 | 6.50 | 0.16 | 0.04 |

photocatalytic activity of Co-N-C/SA-PDI, the radical trapping experiments (Fig. S17a) were carried out by introducing isopropyl alcohol (IPA), p-benzoquinone (p-BQ) and potassium iodide (KI) as the scavengers of $\bullet\text{OH}$, superoxide radicals ($\bullet\text{O}_2^-$) and photogenerated holes (h^+), respectively [10,52,53]. The addition of KI remarkably suppresses the degradation rate of Co-N-C/SA-PDI-70%, and the presence of p-BQ or IPA inhibits the degradation efficiency to some degree. It can be found that the contribution ratio of each reactive species follows the order of $h^+ > \bullet\text{O}_2^- > \bullet\text{OH}$ (Fig. S17b), verifying that h^+ is the dominant reactive species while $\bullet\text{O}_2^-$ and $\bullet\text{OH}$ also participate in photocatalytic reactions. Electron spin resonance (ESR) was used to further confirm the generation of reactive species in Co-N-C/SA-PDI heterostructure. After illumination, Co-N-C/SA-PDI-70% shows stronger 1:2:2:1 signal of $\bullet\text{OH}$ than SA-PDI (Fig. 8a), which should be due to plenty of $\bullet\text{OH}$ generated via the Fenton-like reaction between Co^{2+} in Co-N-C and H_2O_2 in-situ produced by composite photocatalyst as shown in Eq. (1) [54,55]. As shown in Fig. 8b and c, compared to SA-PDI, Co-N-C/SA-PDI-70% exhibits more significant signals of $\bullet\text{O}_2^-$ and $^1\text{O}_2$ under visible light,

demonstrating the increased production of $^1\text{O}_2$ and $^1\text{O}_2$ in the composite system. As observed in Fig. 8d, Co-N-C/SA-PDI-70% exhibits a more distinct decreased triple signal of photogenerated electrons (e^-) after illumination than SA-PDI, demonstrating a larger number of e^- can survive in the heterostructure to react with the adsorbed O_2 for more production of H_2O_2 and $\bullet\text{O}_2^-$ [56,57]. The above discussion manifests h^+ , $\bullet\text{O}_2^-$, $^1\text{O}_2$ and $\bullet\text{OH}$ are the reactive species participated in the visible-light photocatalytic process of Co-N-C/SA-PDI.



On the basis of aforementioned discussion, the photocatalytic mechanism of Co-N-C/SA-PDI composite system for pollutant degradation, H_2O_2 production and disinfection was proposed in Scheme 3. Initially, photoinduced e^- and h^+ are formed on the conduction band (CB) and valence band (VB) of SA-PDI supramolecular photocatalyst excited by visible light, respectively. The π - π interaction between π -electron conjugation system of SA-PDI and N-rich carbonaceous skeleton of Co-N-C is beneficial to promoting the interlayer electron migration from SA-PDI to Co-N-C along the direction of π - π stacking. Besides, due to the double effect of doped N species and imbedded Co nanoparticles existed in carbonaceous motif on altering Fermi energy level, e^- on the CB of SA-PDI can rapidly transfer to Co-N-C via the heterogeneous interface [26,28]. Subsequently, the cumulative photo-induced e^- in the composite surface tends to reduce adsorbed molecular O_2 for more generation of $\bullet\text{O}_2^-$ and H_2O_2 , leading to the enhanced photocatalytic H_2O_2 production activity of Co-N-C/SA-PDI [56]. Meanwhile, $^3\text{O}_2$ is converted into $^1\text{O}_2$ through an energy-transfer (EnT) process [10]. Additionally, a small number of Co^{2+} presented in Co-N-C

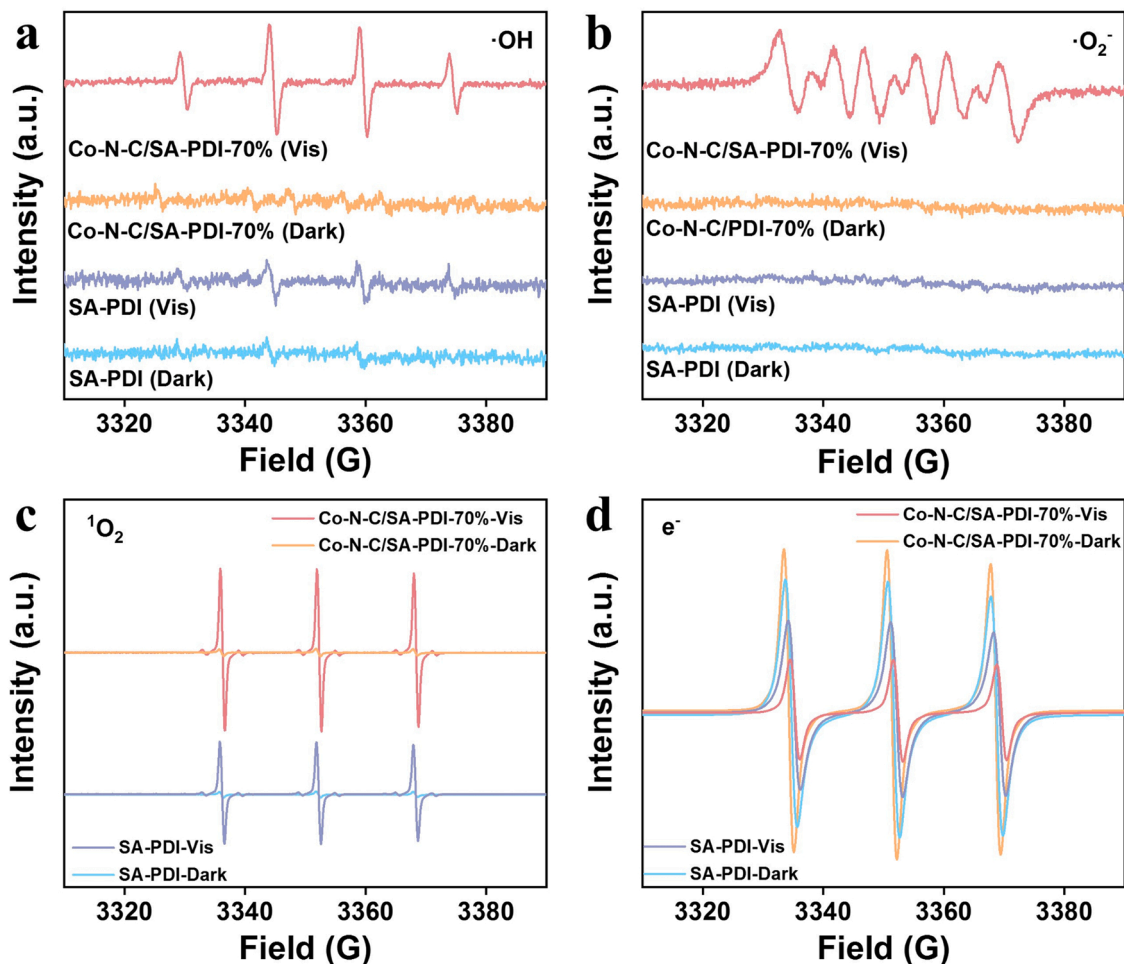
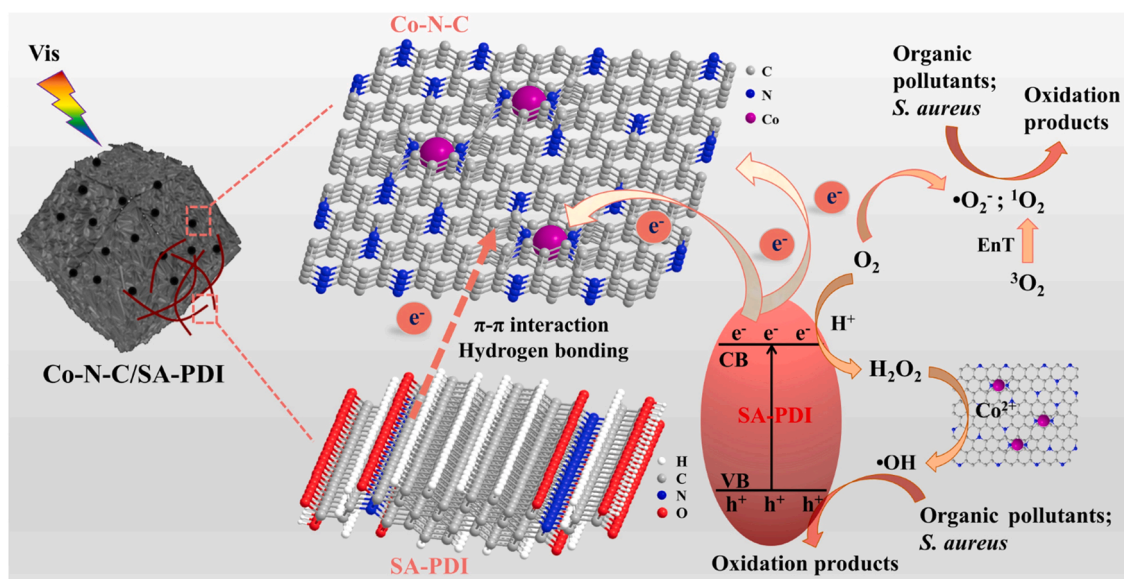


Fig. 8. ESR spectra of SA-PDI and Co-N-C/SA-PDI-70% without and with visible light for the detection of (a) $\bullet\text{OH}$, (b) $\bullet\text{O}_2$, (c) $^1\text{O}_2$ and (d) e^- .



Scheme 3. The proposed photocatalytic mechanism in Co-N-C/SA-PDI composite system under visible light.

can react with in-situ synthesized H_2O_2 from Co-N-C/SA-PDI, leading to the generation of $\bullet\text{OH}$ via Fenton-like reaction. Furthermore, the photoinduced h^+ with high oxidation capacity is accumulated on the VB of SA-PDI. Under the joint action of h^+ , $\bullet\text{O}_2^-$, $^1\text{O}_2$ and $\bullet\text{OH}$,

Co-N-C/SA-PDI displays high-efficiency removal rate towards organic pollutants as well as *S. aureus* cells. The significantly boosted visible photocatalytic performance of Co-N-C/SA-PDI is mainly owing to the following four reasons. (1) The wide-spectrum responsive property of

Co-N-C can efficiently strengthen light-harvesting capacity and broaden spectral response range of the composite, producing more photoinduced carriers participated in photocatalysis. (2) The 3D carbonaceous framework of Co-N-C can significantly improve the surface area and porosity of the heterostructure to produce larger number of reactive sites for pollutant adsorption and multidimensional channels for mass transport and carriers transfer. (3) The π - π interaction between SA-PDI and Co-N-C can be conducive to facilitating the interfacial charge separation, while N-doped carbonaceous matrix and imbedded Co nanoparticles can serve as electron traps to facilitate the interfacial carriers migration. (4) More reactive species (h^+ , $\bullet O_2^-$, 1O_2 and $\bullet OH$) can be produced in the photocatalytic process, dramatically enhancing the oxidation capacity of Co-N-C/SA-PDI composite.

4. Conclusion

In summary, a novel magnetically separable Co-N-C/SA-PDI photocatalyst was successfully prepared through a facile in-situ self-assembly strategy. Co-N-C framework had a close combination with SA-PDI nanofibers to construct a 3D/1D heterostructure via π - π interaction and hydrogen bonds. The strong synergistic action between SA-PDI and Co-N-C co-catalyst reinforced the optical utilization, promoted the carrier transfer, increased the adsorption capacity and improved the recycling ability of the composite. Therefore, compared to SA-PDI and Co-N-C, Co-N-C/SA-PDI displayed extremely boosted photocatalytic performances towards pollutant degradation, disinfection and H_2O_2 production. This work not only provides a novel route to design high-efficiency SA-PDI-based photocatalysts, but also extends the application potential of ZIF-derived co-catalyst in energy conversion and environmental purification.

CRedit authorship contribution statement

Lufang Ning: Methodology, Validation, Formal analysis, Investigation, Data curation, Writing – original draft, Visualization. **Xue Chen:** Methodology, Validation. **Zhouping Wang:** Resources, Supervision, Funding acquisition. **Jing Xu:** Conceptualization, Methodology, Investigation, Resources, Writing – review & editing, Supervision, Project administration, Funding acquisition.

Declaration of Competing Interest

The authors declare that they have no known competing financial interests or personal relationships that could have appeared to influence the work reported in this paper.

Data availability

Data will be made available on request.

Acknowledgments

This work was supported by the Natural Science Foundation of Jiangsu Province (BK20221541), Jiangsu Agriculture Science and Technology Innovation Fund (CX(20)3108), National Natural Science Foundation of China (21707052, 31871881), Fundamental Research Funds for the Central Universities (JUSRP11905).

Appendix A. Supplementary material

Supplementary data associated with this article can be found in the online version at [doi:10.1016/j.apcatb.2022.122282](https://doi.org/10.1016/j.apcatb.2022.122282).

References

- [1] F. Qaderi, A.H. Sayahzadeh, F. Azizpour, P. Vosoghi, Efficiency modeling of serial stabilization ponds in treatment of phenolic wastewater by response surface methodology, *Int. J. Environ. Sci. Technol.* 16 (2019) 4193–4202.
- [2] S. Almeida, A. Raposo, M. Almeida-Gonzalez, C. Carrascosa, Bisphenol A: food exposure and impact on human health, *Compr. Rev. Food Sci. Food Saf.* 17 (2018) 1503–1517.
- [3] E. Sanganyado, W. Gwenzi, Antibiotic resistance in drinking water systems: occurrence, removal, and human health risks, *Sci. Total Environ.* 669 (2019) 785–797.
- [4] R. Lulijwa, E.J. Rupia, A.C. Alfaro, Antibiotic use in aquaculture, policies and regulation, health and environmental risks: a review of the top 15 major producers, *Rev. Aquac.* 12 (2020) 640–663.
- [5] U. Farooq, M.W. Ullah, Q. Yang, A. Aziz, J. Xu, L. Zhou, S. Wang, High-density phage particles immobilization in surface-modified bacterial cellulose for ultra-sensitive and selective electrochemical detection of *Staphylococcus aureus*, *Biosens. Bioelectron.* 157 (2020), 112163.
- [6] N. Lv, Y. Li, Z. Huang, T. Li, S. Ye, D.D. Dionysiou, X. Song, Synthesis of GO/TiO₂/Bi₂WO₆ nanocomposites with enhanced visible light photocatalytic degradation of ethylene, *Appl. Catal. B Environ.* 246 (2019) 303–311.
- [7] X. Chen, Y. Kondo, S. Li, Y. Kuwahara, K. Mori, D. Zhang, C. Louis, H. Yamashita, Visible-light-driven hydrogen peroxide production from water and dioxygen by perylenetetracarboxylic diimide modified titanium-based metal-organic frameworks, *J. Mater. Chem. A* 9 (2021) 26371–26380.
- [8] Z. Wei, M. Liu, Z. Zhang, W. Yao, H. Tan, Y. Zhu, Efficient visible-light-driven selective oxygen reduction to hydrogen peroxide by oxygen-enriched graphitic carbon nitride polymers, *Energy Environ. Sci.* 11 (2018) 2581–2589.
- [9] Z. Zhang, Y. Zhu, X. Chen, H. Zhang, J. Wang, A full-spectrum metal-free porphyrin supramolecular photocatalyst for dual functions of highly efficient hydrogen and oxygen evolution, *Adv. Mater.* 31 (2019) 1806626.
- [10] J. Xu, Q. Gao, Z. Wang, Y. Zhu, An all-organic OD/2D supramolecular porphyrin/g-C₃N₄ heterojunction assembled via pi-pi interaction for efficient visible photocatalytic oxidation, *Appl. Catal. B Environ.* 291 (2021), 120059.
- [11] V. Kunz, V. Stepanenko, F. Wuerthner, Embedding of a ruthenium(II) water oxidation catalyst into nanofibers via self-assembly, *Chem. Commun.* 51 (2015) 290–293.
- [12] D. Liu, J. Wang, X. Bai, R. Zong, Y. Zhu, Self-assembled PDINH supramolecular system for photocatalysis under visible light, *Adv. Mater.* 28 (2016) 7284–7290.
- [13] Y. Zhang, D. Wang, W. Liu, Y. Lou, Y. Zhang, Y. Dong, J. Xu, C. Pan, Y. Zhu, Create a strong internal electric-field on PDI photocatalysts for boosting phenols degradation via preferentially exposing pi-conjugated planes up to 100%, *Appl. Catal. B Environ.* 300 (2022), 120762.
- [14] Y. Pu, F. Bao, D. Wang, X. Zhang, Z. Guo, X. Chen, Y. Wei, J. Wang, Q. Zhang, The asymmetrical-structure of supramolecular precursor to improve internal electric field for simultaneously enhancing contaminant degradation and H_2O_2 production performance, *J. Environ. Chem. Eng.* 10 (2022), 107123.
- [15] J. Wang, W. Shi, D. Liu, Z. Zhang, Y. Zhu, D. Wang, Supramolecular organic nanofibers with highly efficient and stable visible light photooxidation performance, *Appl. Catal. B Environ.* 202 (2017) 289–297.
- [16] Q. Xiang, J. Yu, M. Jaroniec, Preparation and enhanced visible-light photocatalytic H_2 -production activity of graphene/C₃N₄ composites, *J. Phys. Chem. C* 115 (2011) 7355–7363.
- [17] A. Iwase, H. Kato, A. Kudo, Nanosized Au particles as an efficient cocatalyst for photocatalytic overall water splitting, *Catal. Lett.* 108 (2006) 7–10.
- [18] S. Chen, D.L. Jacobs, J. Xu, Y. Li, C. Wang, L. Zang, 1D nanofiber composites of perylene diimides for visible-light-driven hydrogen evolution from water, *RSC Adv.* 4 (2014) 48486–48491.
- [19] W. Wei, Z. Wei, D. Liu, Y. Zhu, Enhanced visible-light photocatalysis via back-electron transfer from palladium quantum dots to perylene diimide, *Appl. Catal. B Environ.* 230 (2018) 49–57.
- [20] J.T. Kirner, J.J. Stracke, B.A. Gregg, R.G. Finke, Visible-light-assisted photoelectrochemical water oxidation by thin films of a phosphonate-functionalized perylene diimide plus CoOx cocatalyst, *ACS Appl. Mater. Interfaces* 6 (2014) 13367–13377.
- [21] W. Li, H. Chen, Y. Liu, T. Cai, W. Dong, X. Xia, A novel Ti₃C₂ MXene/PDI supramolecules composite with enhanced photocatalytic activities for degradation of tetracycline hydrochloride under visible-light, *J. Environ. Chem. Eng.* 10 (2022), 107978.
- [22] N.L. Torad, M. Hu, S. Ishihara, H. Sukegawa, A.A. Belik, M. Imura, K. Ariga, Y. Sakka, Y. Yamauchi, Direct synthesis of MOF-derived nanoporous carbon with magnetic Co nanoparticles toward efficient water treatment, *Small* 10 (2014) 2096–2107.
- [23] Y. Zhang, J. Xu, J. Zhou, L. Wang, Metal-organic framework-derived multifunctional photocatalysts, *Chin. J. Catal.* 43 (2022) 971–1000.
- [24] J. Wang, Q. Xu, M. Liu, K. Wang, Z. Wang, P. Qu, The synergistic effect of N, S-codoped carbon and CoOx nanodots derived from ZIF-67 as a highly efficient cocatalyst over CdS nanorods, *Sustain. Energy Fuels* 4 (2020) 1954–1962.
- [25] Q. Mu, W. Zhu, G. Yan, Y. Lian, Y. Yao, Q. Li, Y. Tian, P. Zhang, Z. Deng, Y. Peng, Activity and selectivity regulation through varying the size of cobalt active sites in photocatalytic CO₂ reduction, *J. Mater. Chem. A* 6 (2018) 21110–21119.
- [26] L. Ning, J. Xu, Y. Lou, C. Pan, Z. Wang, Y. Zhu, A 3D/OD cobalt-embedded nitrogen-doped porous carbon/supramolecular porphyrin magnetic-separation photocatalyst with highly efficient pollutant degradation and water oxidation performance, *J. Mater. Sci. Technol.* 124 (2022) 53–64.

- [27] X. Li, C. Zeng, J. Jiang, L. Ai, Magnetic cobalt nanoparticles embedded in hierarchically porous nitrogen-doped carbon frameworks for highly efficient and well-recyclable catalysis, *J. Mater. Chem. A* 4 (2016) 7476–7482.
- [28] J.L. Chang, Y.F. Wang, L.M. Chen, D.P. Wu, F. Xu, Z.Y. Bai, K. Jiang, Z.Y. Gao, Cobalt nanoparticles embedded nitrogen doped carbon, preparation from alkali deprotonation assisted ZIF-67 and its electrocatalytic performance in oxygen evolution reaction, *Int. J. Hydrog. Energy* 45 (2020) 12787–12797.
- [29] D. Wang, Y. Li, Y. Jiang, X. Cai, X. Yao, Perspectives on surface chemistry of nanostructured catalysts for heterogeneous advanced oxidation processes, *Environ. Funct. Mater.* 1 (2022) 182–186.
- [30] J. Yang, H. Miao, Y. Wei, W. Li, Y. Zhu, pi-pi Interaction between self-assembled perylene diimide and 3D graphene for excellent visible-light photocatalytic activity, *Appl. Catal. B Environ.* 240 (2019) 225–233.
- [31] K. Zhu, M. Zhang, X. Feng, L. Qin, S.Z. Kang, X. Li, A novel copper-bridged graphitic carbon nitride/porphyrin nanocomposite with dramatically enhanced photocatalytic hydrogen generation, *Appl. Catal. B Environ.* 268 (2020), 118434.
- [32] H. Meng, Y. Liu, H. Liu, S. Pei, X. Yuan, H. Li, Y. Zhang, ZIF67@MFC-derived Co/N-C@CNFs interconnected frameworks with graphitic carbon-encapsulated Co nanoparticles as highly stable and efficient electrocatalysts for oxygen reduction reactions, *ACS Appl. Mater. Interfaces* 12 (2020) 41580–41589.
- [33] W. Zeng, T. Cai, Y. Liu, L. Wang, W. Dong, H. Chen, X. Xia, An artificial organic-inorganic Z-scheme photocatalyst $\text{WO}_3/\text{Cu@PDI}$ supramolecular with excellent visible light absorption and photocatalytic activity, *Chem. Eng. J.* 381 (2020), 122691.
- [34] C. Bie, B. Zhu, F. Xu, L. Zhang, J. Yu, In situ grown monolayer N-doped graphene on CdS hollow spheres with seamless contact for photocatalytic CO_2 reduction, *Adv. Mater.* 31 (2019) 1902868.
- [35] W. Liu, Z. Zhou, Z. Li, Y. Yang, J. Zhao, Y. Zhu, W. Miao, Cobalt phosphide embedded N-doped carbon nanopolyhedral as an efficient cathode electrocatalyst in microbial fuel cells, *J. Environ. Chem. Eng.* 9 (2021), 104582.
- [36] J. Yang, H. Miao, W. Li, H. Li, Y. Zhu, Designed synthesis of a p- $\text{Ag}_2\text{S}/\text{n-PDI}$ self-assembled supramolecular heterojunction for enhanced full-spectrum photocatalytic activity, *J. Mater. Chem. A* 7 (2019) 6482–6490.
- [37] Z. Li, H. He, H. Cao, S. Sun, W. Diao, D. Gao, P. Lu, S. Zhang, Z. Guo, M. Li, R. Liu, D. Ren, C. Liu, Y. Zhang, Z. Yang, J. Jiang, G. Zhang, Atomic Co/Ni dual sites and Co/Ni alloy nanoparticles in N-doped porous Janus-like carbon frameworks for bifunctional oxygen electrocatalysis, *Appl. Catal. B Environ.* 240 (2019) 112–121.
- [38] J. Xu, Z. Wang, Y. Zhu, Enhanced visible-light-driven photocatalytic disinfection performance and organic pollutant degradation activity of porous g- C_3N_4 nanosheets, *ACS Appl. Mater. Interfaces* 9 (2017) 27727–27735.
- [39] J. Xu, Z. Wang, Y. Zhu, Highly efficient visible photocatalytic disinfection and degradation performances of microtubular nanoporous g- C_3N_4 via hierarchical construction and defects engineering, *J. Mater. Sci. Technol.* 49 (2020) 133–143.
- [40] D. Wang, M. Angel Mueses, J.A. Colina Marquez, F. Machuca-Martinez, I. Grcic, R. P. Muniz Moreira, G. Li Puma, Engineering and modeling perspectives on photocatalytic reactors for water treatment, *Water Res.* 202 (2021), 117421.
- [41] Q. Gao, J. Xu, Z. Wang, Y. Zhu, Enhanced visible photocatalytic oxidation activity of perylene diimide/g- C_3N_4 n-n heterojunction via pi-pi interaction and interfacial charge separation, *Appl. Catal. B Environ.* 271 (2020), 118933.
- [42] J. Li, Z. Xia, D. Ma, G. Liu, N. Song, D. Xiang, Y. Xin, G. Zhang, Q. Chen, Improving photocatalytic activity by construction of immobilized Z-scheme $\text{CdS}/\text{Au}/\text{TiO}_2$ nanobelt photocatalyst for eliminating norfloxacin from water, *J. Colloid Interface Sci* 586 (2021) 243–256.
- [43] Z.H. Diao, S.T. Huang, X. Chen, M.Y. Zou, H. Liu, P.R. Guo, L.J. Kong, W. Chu, Peroxymonosulfate-assisted photocatalytic degradation of antibiotic norfloxacin by a calcium-based Ag_3PO_4 composite in water: reactivity, products and mechanism, *J. Clean. Prod.* 330 (2022), 129806.
- [44] M. Chen, W. Chu, Photocatalytic degradation and decomposition mechanism of fluoroquinolones norfloxacin over bismuth tungstate: experiment and mathematic model, *Appl. Catal. B Environ.* 168 (2015) 175–182.
- [45] F. Wang, J. Xu, Z. Wang, Y. Lou, C. Pan, Y. Zhu, Unprecedentedly efficient mineralization performance of photocatalysis-self-Fenton system towards organic pollutants over oxygen-doped porous g- C_3N_4 nanosheets, *Appl. Catal. B Environ.* 312 (2022), 121438.
- [46] J. Xu, Q. Gao, X. Bai, Z. Wang, Y. Zhu, Enhanced visible-light-induced photocatalytic degradation and disinfection activities of oxidized porous g- C_3N_4 by loading Ag nanoparticles, *Catal. Today* 332 (2019) 227–235.
- [47] D. Liu, L. Chen, W. Chen, M. Qin, S. Wei, Enhanced visible-light photocatalytic activity of perylene diimide (PDI) supramolecular nanorods with Pt QDs deposited in situ, *Dalton Trans.* 50 (2021) 4008–4016.
- [48] J. He, X. Wang, S. Jin, Z.Q. Liu, M. Zhu, 2D metal-free heterostructure of covalent triazine framework/g- C_3N_4 for enhanced photocatalytic CO_2 reduction with high selectivity, *Chin. J. Catal.* 43 (2022) 1306–1315.
- [49] L. Ke, P. Li, X. Wu, S. Jiang, M. Luo, Y. Liu, Z. Le, C. Sun, S. Song, Graphene-like sulfur-doped g- C_3N_4 for photocatalytic reduction elimination of UO_2^{2+} under visible light, *Appl. Catal. B Environ.* 205 (2017) 319–326.
- [50] H. Chen, K. Shen, J. Chen, X. Chen, Y. Li, Hollow-ZIF-templated formation of a $\text{ZnO}/\text{C-N-Co}$ core-shell nanostructure for highly efficient pollutant photodegradation, *J. Mater. Chem. A* 5 (2017) 9937–9945.
- [51] W. Liu, P. Wang, J. Chen, X. Gao, H. Che, B. Liu, Y. Ao, Unraveling the mechanism on ultrahigh efficiency photocatalytic H_2O_2 generation for dual-heteroatom incorporated polymeric carbon nitride, *Adv. Funct. Mater.* 32 (2022) 2205119.
- [52] H. Che, X. Gao, J. Chen, J. Hou, Y. Ao, P. Wang, Iodide-induced fragmentation of polymerized hydrophilic carbon nitride for high-performance quasi-homogeneous photocatalytic H_2O_2 production, *Angew. Chem. Int. Ed.* 60 (2021) 25546–25550.
- [53] S.H. Huo, W.T. Gao, P.X. Zhou, Z.P. Deng, Z.G. Han, X.T. Cui, X.Q. Lu, Magnetic porous carbon composites for rapid and highly efficient degradation of organic pollutants in water, *Adv. Powder Mater.* 1 (2022), 100028.
- [54] X. Yao, Q. Lin, L. Zeng, J. Xiang, G. Yin, Q. Liu, Degradation of humic acid using hydrogen peroxide activated by $\text{CuO-Co}_3\text{O}_4/\text{AC}$ under microwave irradiation, *Chem. Eng. J.* 330 (2017) 783–791.
- [55] X. Li, S. Huang, H. Xu, Y. Deng, Z. Wang, Z.Q. Liu, Molybdenum phosphide (MoP) with dual active sites for the degradation of diclofenac in Fenton-like system, *Chin. Chem. Lett.* 33 (2022) 1321–1324.
- [56] M. Li, W. He, Y. Liu, H. Wu, W.G. Wamer, Y.M. Lo, J.J. Yin, FD&C Yellow No. 5 (Tartrazine) degradation via reactive oxygen species triggered by TiO_2 and Au/TiO_2 nanoparticles exposed to simulated sunlight, *J. Agric. Food Chem.* 62 (2014) 12052–12060.
- [57] S. Lan, X. Ke, Z. Li, L. Mai, M. Zhu, E.Y. Zeng, Piezoelectric disinfection of water Co-polluted by bacteria and microplastics energized by water flow, *ACS ES&T Water* 2 (2022) 367–375.